



# Microstructure and Mechanical Properties of Laser Welded Joints of DZ125L and IN718 Nickel Base Superalloys

Taoshan Liang<sup>1</sup> · Lei Wang<sup>1</sup> · Yang Liu<sup>1</sup> · Xiu Song<sup>1</sup>

Received: 16 August 2017 / Accepted: 26 November 2017 / Published online: 13 March 2018  
© The Korean Institute of Metals and Materials 2018

## Abstract

The microstructure and mechanical properties of the laser welded joint of DZ125L and IN718 nickel base superalloys were investigated. The results show that the fusion zone (FZ) mainly consists of fine dendrite structure with fine  $\gamma'$ , Laves phases and MC carbides inhomogeneously distributed. The high welding temperature induces the partial dissolution of  $\gamma'$  in the heat-affected zone (HAZ) of DZ125L and liquation of grain boundaries in both of the HAZs. After post-weld heat treatment (PWHT), fine  $\gamma''$  and  $\gamma'$  phases precipitate in the FZ, IN718 HAZ and IN718 base metal (BM), and fine  $\gamma'$  precipitate in the  $\gamma$  channel of the HAZ and BM of DZ125L. With tensile testing, the joints after PWHT show higher strengths than that of the weaker DZ125L alloy. Plastic deformation mainly concentrates in the weaker DZ125L and the joint finally fails in the DZ125L BM.

**Keywords** Laser welding · Nickel base superalloy · Post-weld heat treatment · Microhardness · Tensile properties

## 1 Introduction

With the higher demanding of thrust-weight ratio for engines, more attentions are paid to reduce the weight of turbines. Welding of turbine blades to the disk, which is also known as blisk [1], is a promising method to replace traditional riveted joint. However, the used materials are usually high alloyed nickel base alloy [2], and it is hard to achieve the fusion welding because of solidification cracking, strain age cracking and grain boundary liquation cracking [3, 4]. A few recent researches reported that these problems can be avoided by selecting proper base alloys and applying appropriate treatments before welding. Firstly, Ahn et al. [5] and Moosavy et al. [6] reported that the dissimilar welding of  $\gamma'$ -strengthened alloy to  $\gamma''$ -strengthened alloy shows better weldability than the welding of single base alloy. The  $\gamma'$ -strengthened alloy is rich in Al and Ti, while the  $\gamma''$ -strengthened alloy is rich in Nb. During welding, the contents of Al, Ti and Nb in the fusion zone (FZ) were diluted. The dilution of these elements can reduce the

amount of low melting eutectics ( $\gamma$ -Laves,  $\gamma$ -MC and  $\gamma$ - $\gamma'$  eutectics), and then the solidification temperature range decreases accordingly which finally reduce the solidification cracking tendency. The lower solidification cracking tendency makes the fusion welding easier to control. Secondly, Sidhu et al. [7] reported that the directionally solidified nickel base superalloy displays less tendency of strain age cracking during welding. The blade used alloy usually has high Al+Ti content and easily precipitates  $\gamma'$  phases. This makes the alloy susceptible to strain age cracking in the HAZ [8]. Since the directionally solidified alloy has less grain boundaries area per unit volume, the strain age cracking can be obviously reduced, while the single crystal alloy did not crack at all. And thirdly, the  $\gamma''$ -strengthened alloy is prone to liquation cracking in the HAZ due to the remelting of low melting point phases in the grain boundaries and constitutional liquation of Nb carbides during welding. Cao et al. [9] reported that solution treatment before welding can reduce the liquation cracking. Even though, it remains a challenge to weld the high alloyed blade used DZ125L and disk used IN718 nickel base alloys using traditional fusion welding technologies.

Laser beam welding (LBW), as a new fusion welding technology, has high power density, high precision, high welding speed, good flexibility and can provide sound welded joint with narrow weld geometry, large depth/width ratio, narrow

✉ Yang Liu  
liuyang@mail.neu.edu.cn

<sup>1</sup> School of Materials Science and Engineering, Northeastern University, No. 11 Lane 3, Wenhua Road, Heping District, Shenyang 110819, China

heat-affected zone (HAZ) and low distortion [10]. Due to such advantages, laser welding has received considerably more attention in recent years [4]. The recent reports on the laser welding of nickel base alloy show that solidification cracks can be avoided by adjusting the laser welding parameters [11]. LBW can also provide welded joint with less element segregation and harmful phases such as Laves phases [12]. Therefore, it is promising to weld the directionally solidified  $\gamma'$ -strengthened nickel base alloy to the  $\gamma''$ -strengthened nickel base alloy using laser welding. Nevertheless, there is no study reported on this issue.

For these reasons above, we studied the dissimilar laser welding of blade used DZ125L (strengthened mainly by  $\gamma'$ -Ni<sub>3</sub>Al) and disk used IN718 alloy (strengthened mainly by  $\gamma''$ -Ni<sub>3</sub>Nb) and obtained the joint with a joint efficiency about 110% when compared with the weaker base alloy. The joint with optimum welding parameter is reported in this paper. The main objective of the present study is to investigate the as-welded (AW) and post-weld heat treatment (PWHT) microstructure of the laser welded joint of DZ125L and IN718 alloys, and discuss the effects of microstructures on the microhardness and tensile properties of the welded joint.

## 2 Experimental

The nominal compositions of DZ125L and IN718 are listed in Table 1. Before welding, the two alloys were heat treated as follows: 1220 °C/2 h/AC + 1080 °C/4 h/AC + 900 °C/16 h/AC for DZ125L slabs, and 1020 °C/1 h/AC for IN718 slabs (AC: air cooling). Then both of DZ125L and IN718 slabs were sliced into the same dimension, mechanical polished and chemical cleaned. The dissimilar welding was performed using a high-power IPG Photonics YLS-6000 fiber laser system in a butt joint configuration. The welding trials were carried out in a single pass with the laser power of 1600 W, welding speed of 2.1 m/min, focal length of 250 mm, defocus length of -8 mm and shielding gas flow rate of 15 L/min, respectively. The PWHT was carried out at 720 °C/8 h/FC + 620 °C/8 h/AC (FC: furnace cooling).

The specimens for microstructure examination were wire cut along the transverse section of the welded joint, and then followed by mechanical polishing and electro polishing with a solution of 15 g CrO<sub>3</sub> + 10 mL H<sub>2</sub>SO<sub>4</sub> + 150 mL H<sub>3</sub>PO<sub>4</sub>. The microstructures were examined by both OLYMPUS GX71 optical microscope (OM) and JEOL 7001 field emission scanning electron microscope (FESEM) with energy dispersive spectrometer (EDS). The macroscopic distribution of alloying

elements was examined by a SHIMADZU 1610 electron probe micro-analyzer (EPMA). The microstructures were also analyzed using electron backscatter diffraction (EBSD) techniques operated at 20 kV with a spatial step size of 2  $\mu$ m. Channel 5 software was used to collect and index the Kikuchi band patterns.

Microhardness measurement was performed by a Wilson Wdper 401MVD microhardness tester with a load of 50 g, and a time of 15 s. Tensile samples were wire cut into dog bone with a cross section of 5.0  $\times$  2.1 mm<sup>2</sup> and a gauge length of 10 mm. All side surfaces of the samples were grounded with SiC paper through 2000 grit and one side surface in the thickness direction was electro polished before tensile testing for the examination of slip lines after deformation. Tensile testing was conducted using a MTS 810 material testing machine at the strain rate of 10<sup>-3</sup>/s at room temperature. At least three identical samples were examined for data repeatability.

## 3 Results and Discussions

### 3.1 Microstructure of DZ125L and IN718 Before Welding

Typical SEM micrographs and EDS analysis of DZ125L and IN718 alloys before welding are shown in Fig. 1. It can be seen from Fig. 1a that the DZ125L alloy presents dendritic morphologies with the arm spacing about 400  $\mu$ m. MC carbides and ( $\gamma$  +  $\gamma'$ ) eutectics distributed in the interdendrites (Fig. 1b). The micrograph in higher magnifications in Fig. 1c shows that cubic  $\gamma'$  dispersed in the  $\gamma$  matrix. Figure 1d shows the SEM micrographs of IN718 alloy before welding. It exhibits fine equiaxed grains, and almost all  $\delta$  phases re-dissolve into the matrix except for a few carbides (Fig. 1e). The EDS analysis of carbides in Fig. 1f, g shows that the carbides are MC carbides in both of the alloys. The MC carbide in DZ125L alloy is rich in Ti and Ta while it is rich in Nb in IN718 alloy.

### 3.2 AW Microstructure of Dissimilar DZ125L/IN718 Welded Joint

#### 3.2.1 AW Microstructure in FZ

The overview of the AW joint is shown in Fig. 2a and magnified SEM observations of typical regions are shown in

**Table 1** Nominal chemical compositions of DZ125L and IN718 alloys (wt%)

	C	Cr	Co	Mo	Fe	Al	Ti	Nb	Ta	W	Ni
DZ125L	0.12	8.74	9.54	2.21	–	5.03	3.18	–	3.96	6.46	Bal.
IN718	0.22	17.98	0.14	2.96	17.52	0.52	1.00	5.39	–	–	Bal.

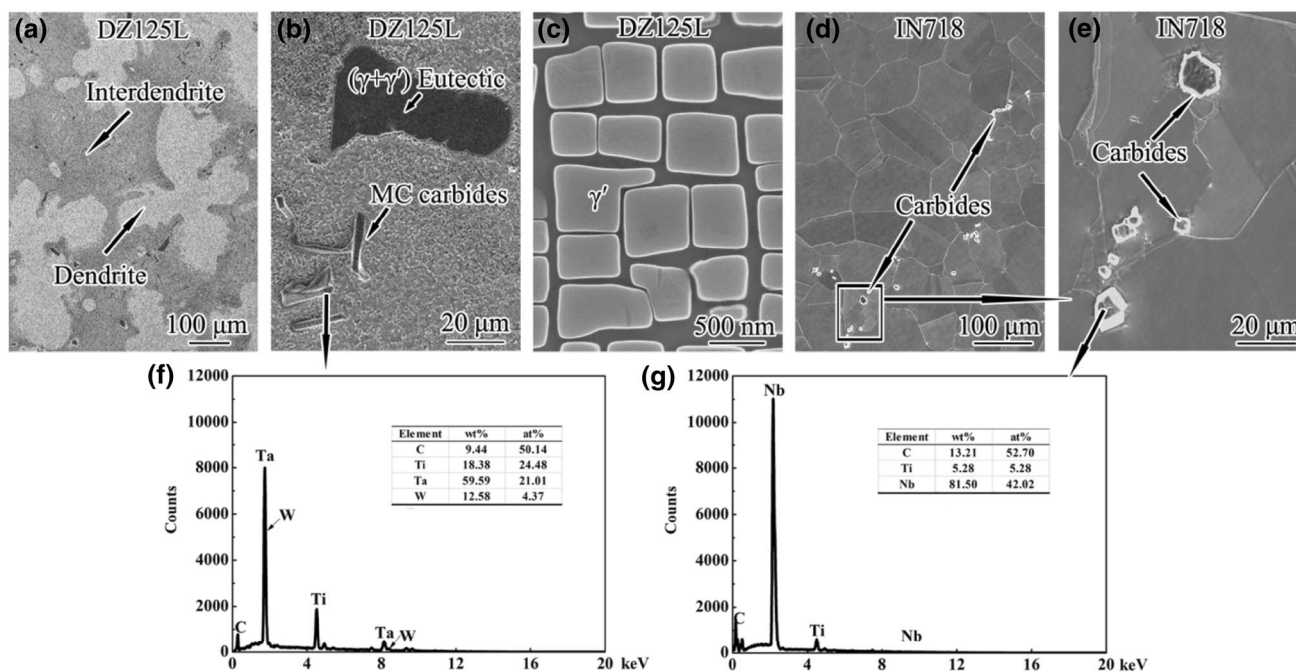


**Fig. 1** SEM micrographs and EDS analysis showing the microstructure of the DZ125L alloy and IN718 alloy before welding **a** DZ125L alloy, **b** MC carbides and eutectics in the interdendrites of DZ125L

alloy, **c** cubic  $\gamma'$  in the  $\gamma$  matrix of DZ125L alloy, **d** IN718 alloy, **e** carbides in IN718, **f** EDS of carbides in DZ125L, and **g** EDS of carbides in IN718

**Fig. 2c–g.** The FZ is funnel-shaped and the grains in the FZ consist mainly of columnar dendrites with arm spacing of 5–10  $\mu\text{m}$  which is much smaller than that of the base metal (BM) of DZ125L ( $\sim 400 \mu\text{m}$ ). Since the joint will be used at high temperatures and the grain structure can directly affect the high temperature strength of the alloy, the grain structure in the FZ outlined by yellow line was analyzed by EBSD. The corresponding result is shown in Fig. 2b. It can be seen that the DZ125L consists of 2 columnar  $\langle 001 \rangle$  grains, the IN718 consists of fine-equiaxed grains, while in the FZ, most of the grains are columnar grains. Since the grains in the FZ grow epitaxially on the base metal grains, the number of grains is less in the region near the DZ125L side than that near the IN718 side. Besides, textures are observed in the FZ. In the region marked by I in Fig. 2b, most of the grains are  $\langle 001 \rangle$  grains (red); while for the region II, the number of  $\langle 101 \rangle$  grains (green) and  $\langle 111 \rangle$  grains (blue) increases obviously. Moreover, a curved centerline can be seen in the middle of the FZ which runs through the welded joint.

The elements usually cannot mix completely, and this induces macrosegregation in the FZ [13]. The macrosegregation will further affect the microstructures. Therefore, the distribution of elements across the FZ was analyzed by EPMA linear scanning. The distribution of Al, Ti and Nb that have low equilibrium distribution coefficient  $k$  ( $k < 1$ ) [6, 14, 15] and significant influence on the formation of second phases are listed in Fig. 3. The DZ125L has a relatively higher Al and Ti while the Nb content

is higher in IN718. In the FZ, these elements are diluted by the opposite alloy, and the contents of these elements generally fall in between that of the two alloys. As a result, sudden changes are formed at the fusion lines. The incomplete mixing of DZ125L and IN718 alloys in the FZ results in the Al + Ti rich regions and Nb rich regions side by side. Fine  $\gamma'$  with sizes less than 10 nm are observed in the interdendrite of Al + Ti rich region as shown in the SEM micrographs in Fig. 3, while no precipitation can be observed in the interdendrite of Nb rich regions and other regions. The microsegregation of these elements is supposed to be responsible for this phenomenon. In order to have a quantitative interpretation of the segregation behavior of each element in the FZ, the equilibrium distribution coefficient  $k_x$  of each element was calculated according to the following Eq. (1): [6]

$$k_x = \frac{C_{Core}}{C_{0,x}} \quad (1)$$

where  $k_x$  is the equilibrium distribution coefficient,  $C_{0,x}$  is the nominal composition of  $x$  species,  $C_{Core}$  is the  $x$  composition in the dendrite core. There is a problem when applying this calculation into the current study: the welding is dissimilar welding and there are macrosegregation in the FZ, thus the nominal composition of  $x$  species is unknown in specific location. To solve this problem, the nominal composition of each element was determined by the average chemical

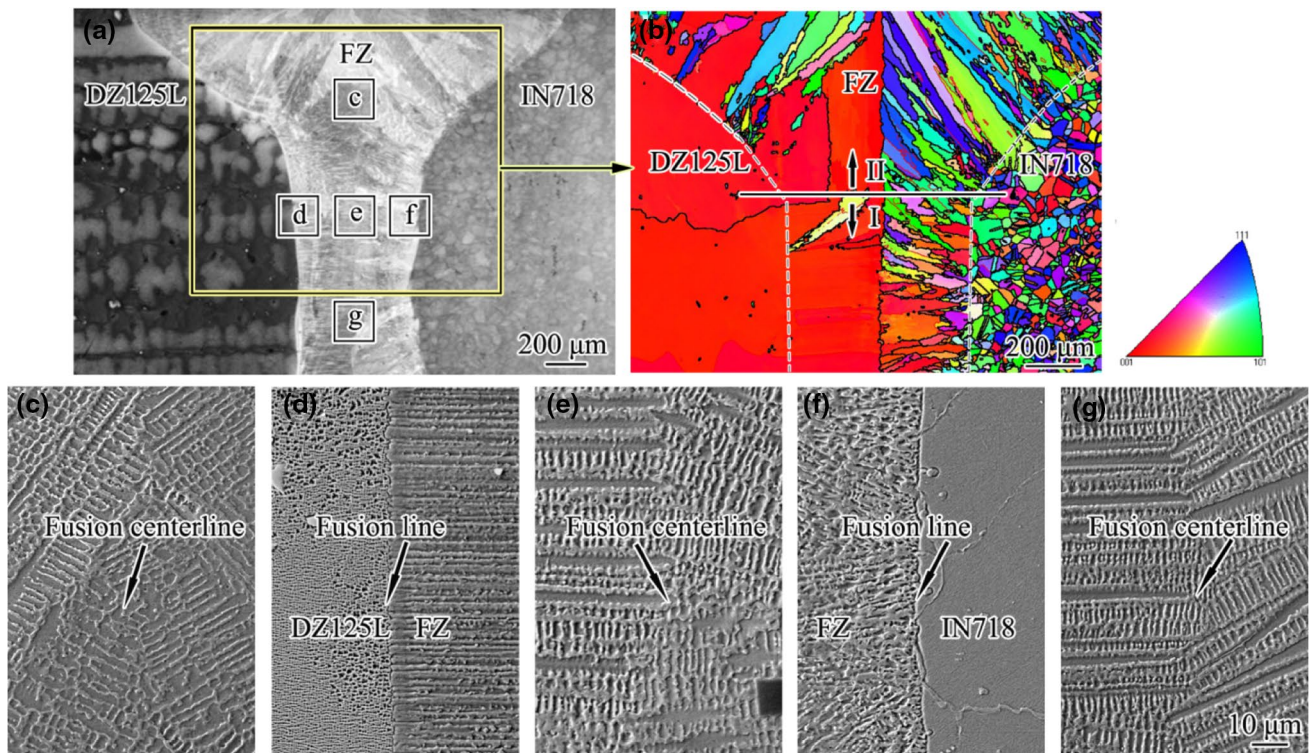


**Fig. 2** OM, EBSD and SEM micrographs showing the microstructures across the dissimilar DZ125L/IN718 welded joint **a** overview of OM; **b** Inverse pole figure (IPF) with grain boundaries: red line

represents 5°–15°, black line represents above 15°; **c, d, e, f** and **g** the magnified micrographs of the regions marked by **c, d, e, f** and **g** in **(a)**. (Color figure online)

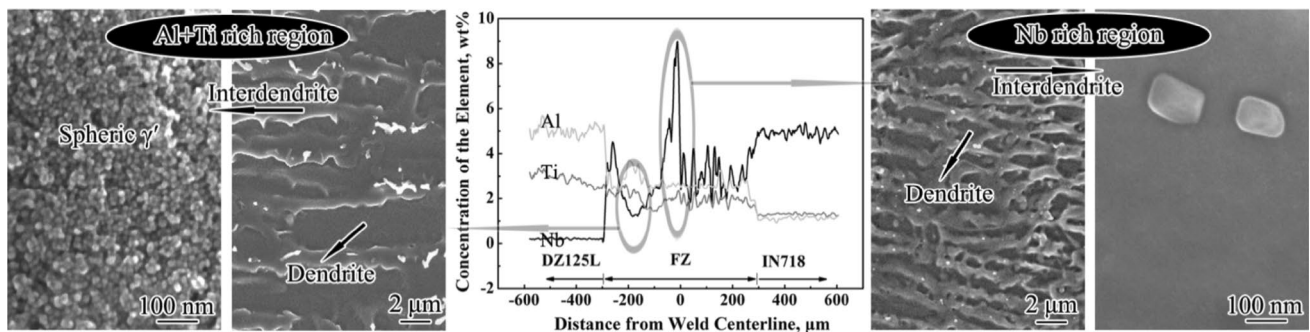


**Fig. 3** EPMA linear scanning of elements Al, Ti and Nb across the AW dissimilar DZ125L/IN718 welded joint and the corresponding microstructures of Al+Ti rich region and Nb rich region

composition in an area of  $5\ \mu\text{m} \times 5\ \mu\text{m}$  which containing both dendrite and interdendrite regions. The element alloying compositions obtained by EPMA and the calculated  $k$  values are listed in Table 2. The result indicates that Cr, Co, Fe, W, Ni with  $k > 1$  are prone to stay at dendrite core, while Al, Mo, Nb, Ti and Ta with  $k < 1$  have higher tendency segregate into the interdendrites. In the Al+Ti rich region, the segregation of Al and Ti to the interdendrite regions makes these regions higher in Al and Ti, and the high content of Al+Ti promotes the precipitation of  $\gamma'$  even under a

high cooling rate during welding. Moreover, the segregation of Nb, Ti, Ta and C promotes the formation of script MC carbide, while the segregation of Mo, Nb and Ti promotes the formation of Laves phase in the interdendrites [16, 17]. Large amounts of carbides and Laves phases are inhomogeneously distributed in the FZ, as shown in Fig. 4. We can see from the EDS analysis that the carbide is rich in Ti, Nb and Ta, while the Laves phase is rich in Nb, Ti and Mo. Because of the fast cooling rate during welding, the sizes of these two phases are small, which are  $\sim 2$  and  $\sim 5\ \mu\text{m}$ , respectively.

**Table 2** Compositions of alloying element obtained by EPMA and the calculated  $k$  values

Element	Al + Ti rich region			Nb rich region			Base alloy	
	$C_{Core}$	$C_{0,x}$	$K_X$	$C_{Core}$	$C_{0,x}$	$K_X$	DZ125L	IN718
Cr	13.72	13.38	1.03	15.73	14.65	1.07	8.74	17.98
Co	6.10	5.35	1.14	3.73	3.52	1.06	9.54	0.14
Fe	8.26	8.10	1.02	11.99	11.68	1.03	–	17.52
W	2.60	2.28	1.14	1.38	1.21	1.14	6.46	–
Ni	59.41	58.51	1.02	58.18	56.93	1.02	60.76	54.27
Al	3.70	3.88	0.95	1.74	1.82	0.96	5.03	0.52
Mo	2.16	2.48	0.87	2.49	2.81	0.89	2.21	2.96
Nb	1.21	2.04	0.59	3.16	5.03	0.63	–	5.39
Ti	1.38	2.17	0.63	1.24	1.90	0.65	3.18	1.00
Ta	1.47	1.82	0.81	0.36	0.45	0.80	3.96	–
C	–	–	0.21–0.30 [19, 28]	–	–	0.21–0.30 [19, 28]	0.12	0.22

### 3.2.2 AW Microstructure in HAZ

Both HAZs are quite narrow and there are no sharp lines dividing the HAZs from the BMs, and the grain growth is not obvious in the HAZ of IN718. Cubic  $\gamma'$  phases partially dissolve in the HAZ of DZ125L, as shown in Fig. 5. Additionally, fine spheric  $\gamma'$  phases are observed in the  $\gamma$  channels. These phenomena are more obvious at the shoulder (Fig. 5b) than that at the bottom regions of the welded joint

(Fig. 5c). The re-dissolution of  $\gamma'$  occurs when the joint is heated to a temperature that exceeds the solution temperature of  $\gamma'$  phases during welding, while the re-precipitation of  $\gamma'$  from the supersaturated solid solution takes place during cooling from the welding temperature. However, there is not enough time for the full dissolution and the growth of the second phase because of the rapid heating and cooling rate. Whereas it is reported that the cooling rate is relatively low at the shoulder of the welded joint [18], which means

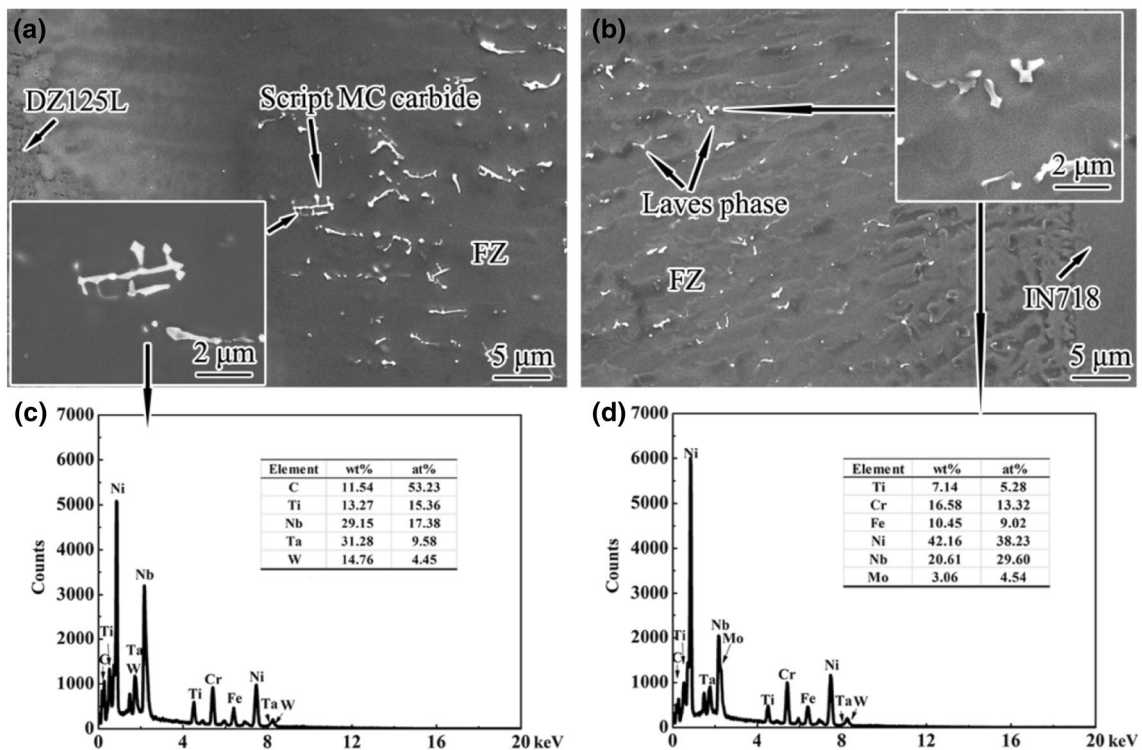


**Fig. 4** SEM micrographs showing heterogeneous distribution of Laves phases and MC carbides in the FZ of the dissimilar DZ125L/IN718 welded joint **a** script MC carbide, **b** Laves phase, **c** EDS of script MC carbide, and **d** EDS of Laves phase

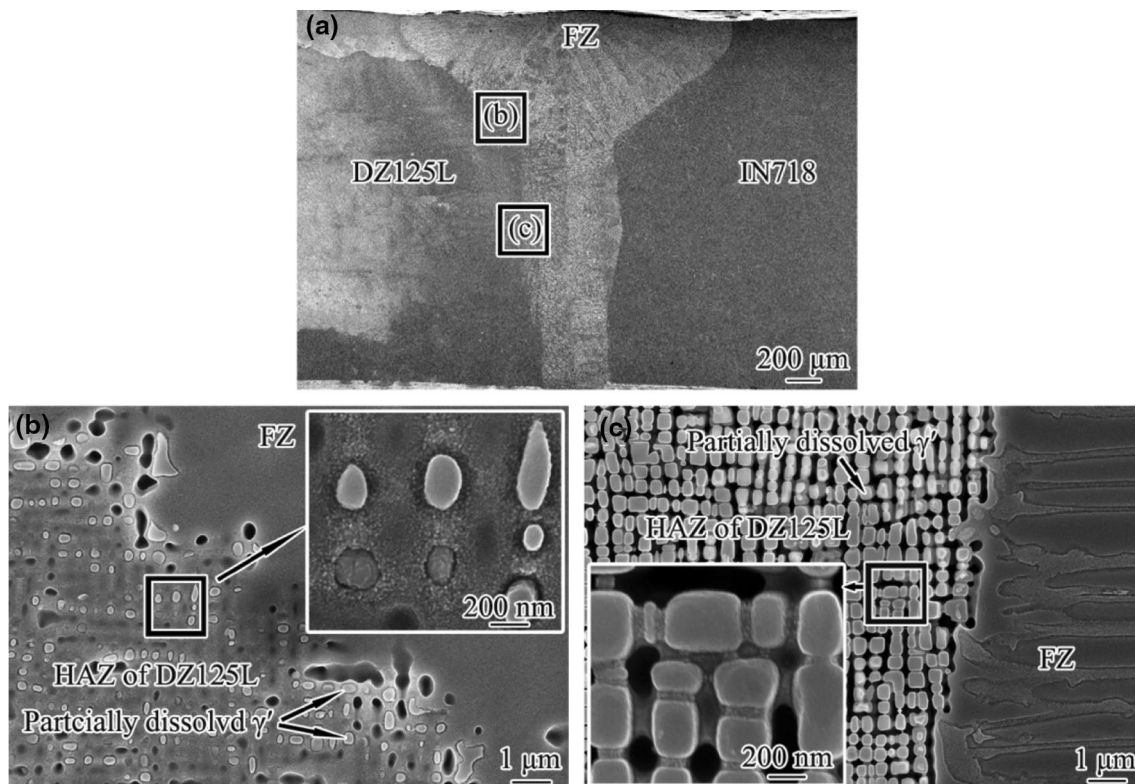


**Fig. 5** SEM micrographs showing the partially re-dissolved  $\gamma'$  in the DZ125L HAZ of the dissimilar DZ125L/IN718 welded joint **a** overview of the welded joint, **b** and **c** magnified micrographs of the region marked by **b** and **c** in (a)

that this region will stay at higher temperature for a longer time period as compared with that of the region shown in Fig. 5c. Therefore, a higher degree of re-dissolution and re-precipitation of  $\gamma'$  phases happen at the shoulder of welded joint during welding.

Liquid boundaries (LBs) are observed in both HAZs near the fusion lines, as shown in Fig. 6. The number of LBs in DZ125L is much less than that of IN718, since DZ125L has less grain boundaries than that of IN718. The liquid boundary is mainly resulted from the remelting of low melting

point phases in the grain boundaries and constitutional liquation of Nb carbides during welding [19]. The major bad effect of boundaries get liquid is the high cracking tendency of the liquid boundaries under the effect of welding thermal stress. In the present welded joint, no obvious crack was observed. However, Laves phases are observed within the LBs in both of the HAZs. It is known that the DZ125L does not contain Nb. Thus the formation of Laves phases in the LBs of DZ125L HAZ implies that not only the remelting of the LBs, but also liquid flow occurs between the FZ and LBs

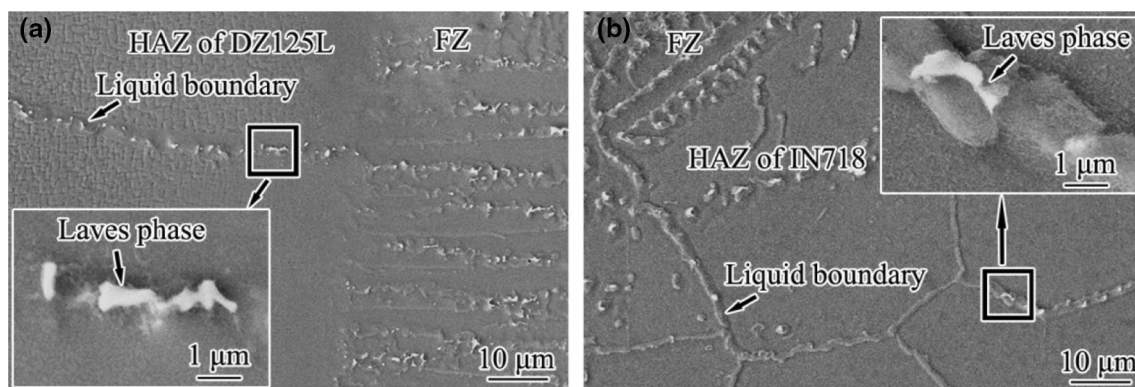


**Fig. 6** SEM micrographs showing the microstructure of the liquid boundaries in the HAZ near the fusion line of **a** DZ125L, and **b** IN718

during welding, by which the element in the FZ can enter into the LBs. The refill of liquid metal may be helpful to heal the potential crack along grain boundaries during welding.

### 3.3 PWHT Microstructure of Dissimilar DZ125L/IN718 Welded Joint

The welded joint cannot be used directly due to the dissolution of strengthening phases. PWHT is a necessary process to precipitate strengthening phases, and restore the mechanical properties of the welded joints. After PWHT, no strain-age cracking is observed in the dissimilar DZ125L/IN718 welded joint. Since the temperature of PWHT in this study is relatively low, the dendrite morphologies, Laves phases and MC carbides have no obvious changes, and the main changes of the microstructures are the precipitation of spherical  $\gamma''$  and  $\gamma'$  phases, as shown in Fig. 7. Since both of these phases are special, it is difficult to recognize those using SEM micrographs. The welded joint was heat treated at 680 °C for 500 h, thus the shape of  $\gamma''$  phases transformed from spheric to disc shape, while the  $\gamma'$  phase remains spheric [20, 21]. We found that  $\gamma''$  phases mainly locate in the interdendrites of Nb rich regions. The reason for no  $\gamma''$  precipitating in other regions can be mainly attributed to the following three factors. First of all, the ratio of (Al+Ti)/Nb is much higher than 0.8 [22], indicating that  $\gamma'$  will precipitates prior to  $\gamma''$  during aging treatment. Secondly, the Nb content is low, while most of it preferentially forms Laves phases and MC carbides. This suggests that there is less Nb to form  $\gamma''$ . And thirdly, there is Ta in these regions which can delay the precipitation of  $\gamma''$  [23]. For these reasons above, the precipitation of  $\gamma''$  phase is inhibited in these regions. The SEM micrographs in Fig. 8 show that fine spheric  $\gamma'$  phases reprecipitate in the  $\gamma$  channels of the BM and the HAZ of DZ125L (Fig. 8a, b). Fine particles precipitate in the grains and along the liquid boundaries in the HAZ of IN718 (Fig. 8c). These fine particles are  $\gamma''$  and  $\gamma'$  phases [24].

### 3.4 Microhardness of Dissimilar DZ125L/IN718 Welded Joint

The microhardness across the AW joint is shown in dark dot line of Fig. 9. The microhardness values of the HAZ of DZ125L are almost equivalent to that of the BM of DZ125L, which are the highest of the welded joint. The value of microhardness decreases rapidly from the HAZ of DZ125L to the FZ. After that, it decreases again at the fusion line adjacent to IN718, and reaches the lowest value of ~250 HV in the HAZ of IN718 (indicated by the black arrow). From the HAZ of IN718 to the BM of IN718, the microhardness increases gradually and finally reaches a relatively higher level.

The variation of microhardness reconfirms the change of microstructure across the AW joint. Since the DZ125L has been pre-weld heat treated, the dispersed distribution of  $\gamma'$  in the matrix contributes to the highest microhardness. The microhardness fluctuations in DZ125L are related to the presence of MC carbides and eutectics in the interdendrite regions, as seen in Fig. 1b. In the FZ,  $\gamma'$  does not fully precipitate because of the rapid cooling rate, thus the microhardness is lower than that of DZ125L. In addition, the heterogeneous distribution of the second phases, i.e. Laves phases, MC carbides and  $\gamma'$ , induce the fluctuation of the microhardness in the FZ. In the HAZ of IN718, more second phases dissolve into the matrix at the peak welding temperature, so the microhardness drops to the lowest level of the AW joint.

After PWHT, the microhardness in all areas recovers to higher levels. Even though the microhardness of the FZ is a bit higher than other regions and the DZ125L has the lowest microhardness, there are no sudden changes at the fusion lines, as shown by the grey dot line in Fig. 9. Based on the microstructure discussed above, it can be analyzed that the increased microhardness in the FZ is mainly caused by the precipitation of fine  $\gamma''$  and  $\gamma'$ . The slight increase in the microhardness of DZ125L can also

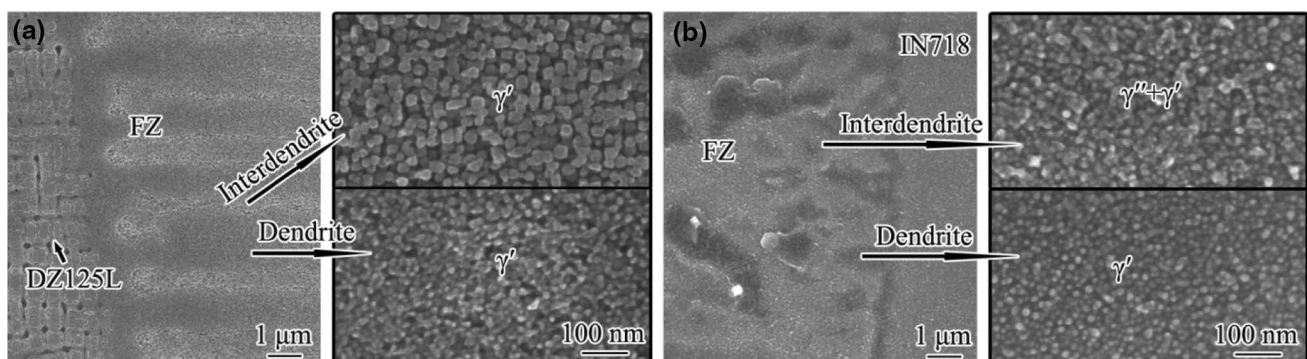


**Fig. 7** SEM micrographs showing the precipitation of  $\gamma''$  and  $\gamma'$  in the FZ of the dissimilar DZ125L/IN718 welded joint after PWHT **a** the region rich in Al+Ti, and **b** the region rich in Nb

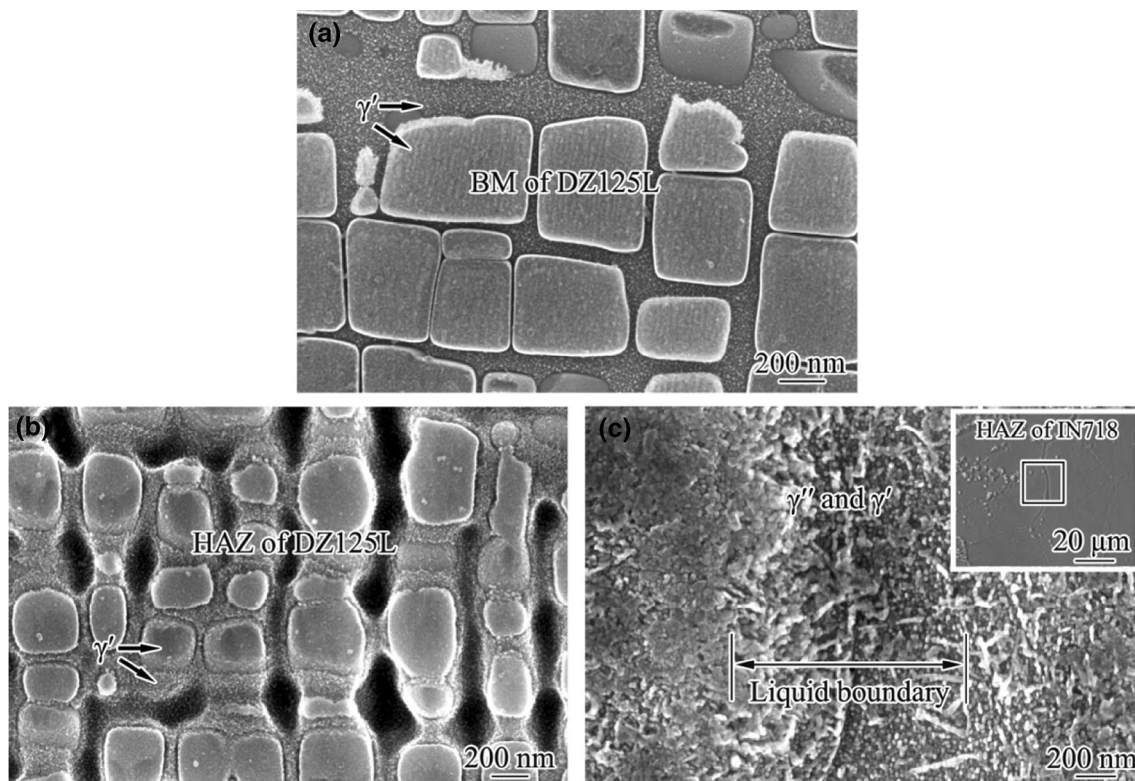


**Fig. 8** SEM micrographs showing the precipitation in different regions of the dissimilar DZ125L/IN718 welded joint after PWHT **a** in the BM of DZ125L, **b** in the HAZ of DZ125L, and **c** along the liquid boundary of the HAZ of IN718

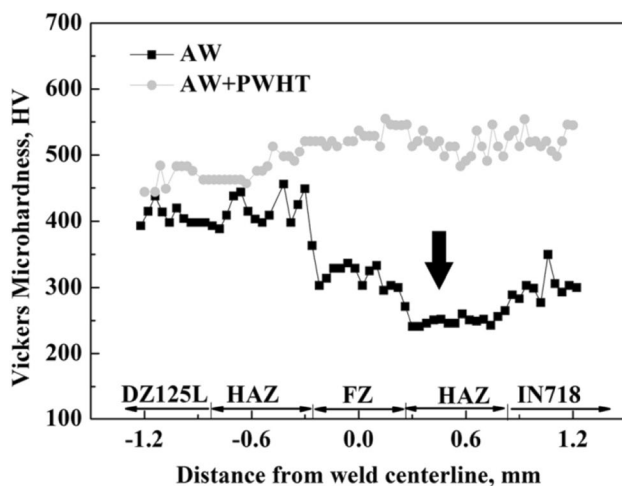


**Fig. 9** Hardness profiles of the dissimilar DZ125L/IN718 welded joint in AW and after PWHT

be attributed to the precipitation of fine spheric  $\gamma'$  in the  $\gamma$  channel. In addition, the increased hardness in the HAZ of IN718 and BM of IN718 is mainly caused by the precipitation of  $\gamma''$  and  $\gamma'$  phases.

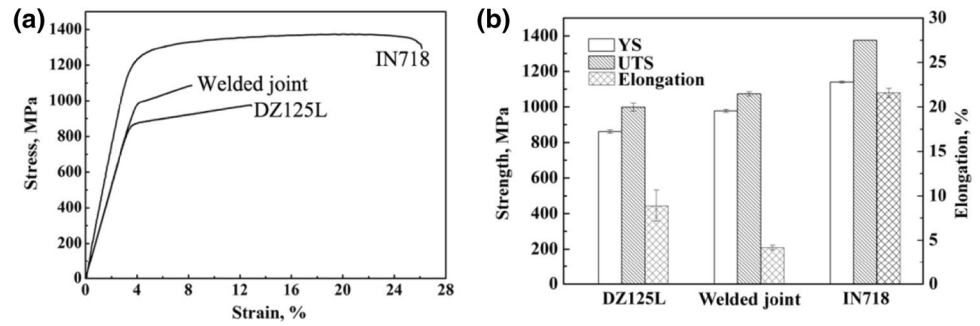
### 3.5 Tensile Behavior of DZ125L, IN718 and the Dissimilar DZ125L/IN718 Welded Joint

The tensile testing of DZ125L, IN718 and the welded joint after PWHT were conducted to further evaluate the effect of microstructure on the tensile properties of the welded joint. Engineering stress–strain curve of each material and the corresponding tensile properties in terms of yield strength (YS), ultimate tensile strength (UTS) and total elongation are shown in Fig. 10. The YS of the welded joint is 977 MPa and it is higher than that of the DZ125L alloy. The UTS of the welded joint is 1074 MPa, which is higher than that of the DZ125L alloy but lower than the YS of the IN718 alloy which is 1140 MPa. The joint efficiency of the welded joint was about 110% when considering the weaker DZ125L BM as the basis for comparison. The total elongation of the welded joint is around half of that of the DZ125L alloy and significantly lower than that of the IN718 alloy. In all cases, the welded joints fail at the weaker BM of DZ125L and the fracture locations are away from the FZ and HAZ of DZ125L (Fig. 11a).

The thicknesses in four different sites after deformation were measured. These four sites are chosen of DZ125L BM near the fracture location, DZ125L BM near the FZ, center of FZ, and IN718 BM near the FZ (arrowed in Fig. 11a).



**Fig. 10** Tensile properties of the DZ125L, IN718 and the dissimilar DZ125L/IN718 welded joint **a** stress–strain curves, and **b** comparison of the tensile properties in terms of YS, UTS and total elongation



The measured values are labeled accordingly in Fig. 11a. It can be seen that all these four sites have reduction in thickness, and the reduction is the highest in the DZ125L and lowest in the FZ. Additionally, slip bands were observed in the FZ and IN718 BM of the welded joint, as shown in Fig. 11c, d. These phenomena indicate that the plastic deformation occurs in all regions of the welded joint, and the FZ is stronger than the DZ125L and IN718 during the tensile deformation. However, it is interesting that even though the UTS of the welded joint is lower than the YS of the IN718 and the FZ is stronger than the IN718, plastic deformation occurs in the FZ and IN718. Localized deformation can be responsible for initiating the plastic deformation in the FZ and IN718. Lun et al. [25] reported that the propagation of Lüders band from one end of the gauge to the other can raise the local strain by approximately 7% under uniaxial tensile

strain. As a result, stress concentration occurs in front of the local strain. With the aid of local strain and stress concentration, the alloy with higher strength can be yielded even the engineering stress is lower than the YS of the alloy. A schematic illustration is given in Fig. 12 to analyze the occurrence of plastic deformation in the FZ and IN718. During the tensile deformation, the loading stress first reaches the yield strength of the DZ125L and the plastic deformation occurs in DZ125L. With the increasing of loading stress, the localized deformation front reaches the fusion line, plastic deformation takes place in the FZ when the stress concentration is high enough (I). Similarly, when the plastic deformation runs through the FZ and reaches the fusion line of the IN718, stress concentration occurs around the fusion line of IN718 (II). Plastic deformation in the IN718 will be initiated when the stress concentration is high enough. When the

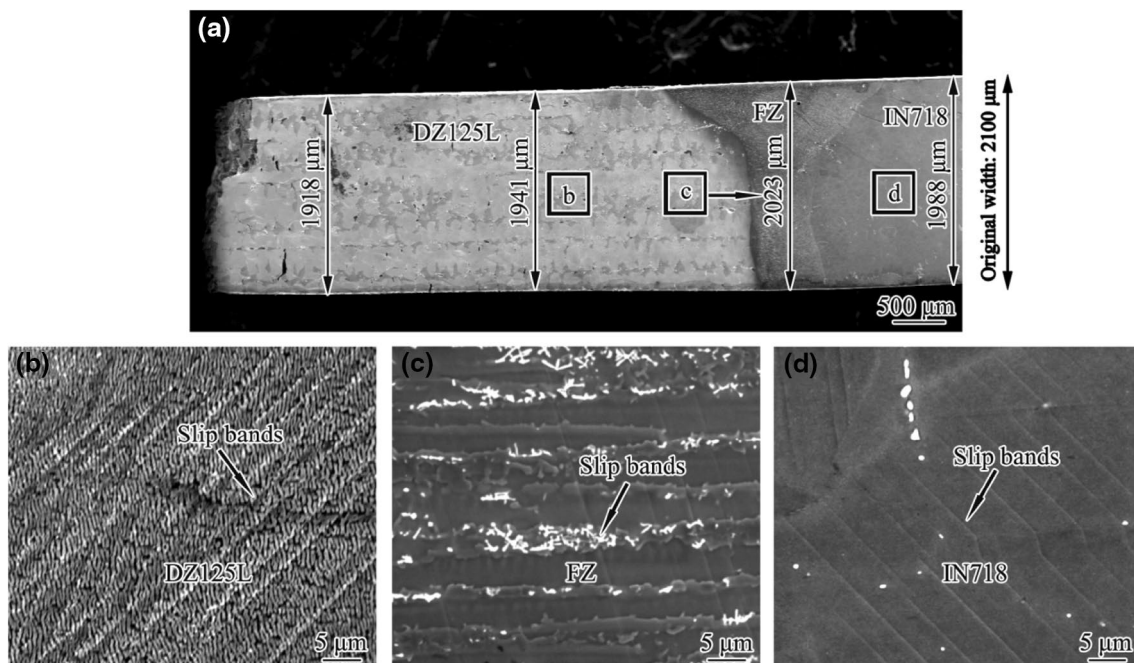


**Fig. 11** SEM micrographs of the side surface microstructure of the dissimilar DZ125L/IN718 welded joint after tensile deformation **a** overview of the welded joint showing the thickness reduction of dif-

ferent regions; **b**, **c** and **d** are the magnification of the microstructures in the regions of **b**, **c** and **d** marked in **(a)** respectively

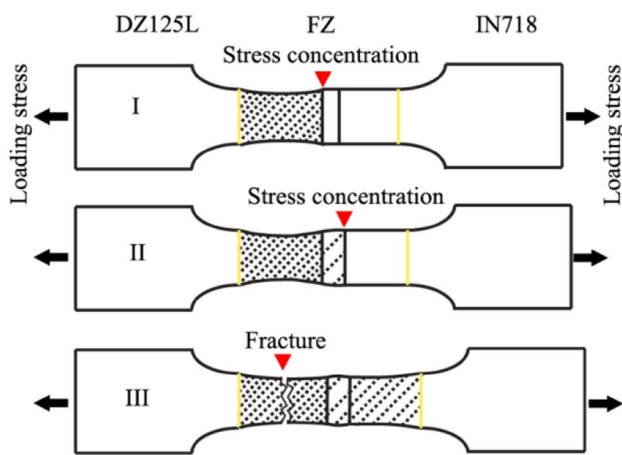


**Fig. 12** Schematic illustration showing the stress concentration in different deformation process when the dissimilar DZ125L/IN718 welded joint under uniaxial tensile loading

loading stress reaches the fracture strength of the DZ125L, the welded joint fails at the DZ125L (III). It is worth noting that even though all the regions, i.e., DZ125L, FZ and IN718 deform plastically, most of the plasticity concentrate in the DZ125L due to its low strength, and because of this, the welded joint shows low ductility.

Figure 13 depicts the SEM micrographs of the typical fracture morphologies of both base alloys and the welded joint. The welded joint fails in the DZ125L, the fracture surface exhibits similar feature with that of the DZ125L base alloy: (1) the fracture surface mainly contains of large cleavage planes and (2) carbides are found on the fracture surfaces. The cleavage planes are resulted from the propagation of cracks encounter the deformation twins and afterwards the cracks propagate along the interface between the

deformation twins [26, 27]. The fracture of IN718 alloy was predominantly characterized by the dimple-like ductile fracture. Thus the IN718 shows better plasticity. Carbides can be observed at the bottom of these dimples. The cross sectional fractures in Fig. 14 show that the carbides in DZ125L broken into pieces which nearly parallel to each other. This indicates that the carbides were broken along the low energy face. The microcracks in the DZ125L alloy originate from the broken of MC carbides. The growth and interaction of these microcracks induce the cleavage fracture of the matrix. While in the IN718 alloy, besides of the broken of carbides itself, debonding of carbides with matrix can be observed as well. The crack propagates transgranularly in the IN718 alloy. The microcracks in IN718 originate from the broken and debonding of MC carbides which forms void. Dimple was initiated by void formation, and then growth and coalescence until the fracture of the alloy.

Generally, the centerline, large amounts of Laves phase and MC carbides in the FZ used to be the weak points. Especially the Laves phase and MC carbide, both of these two phases are brittle and cannot deform coordinately with the matrix. During deformation, the broken or debonding of them with the matrix can make them the crack sources. However, no obvious cracks are observed in these regions after deformation. This implies that Laves phases and MC carbides with small sizes do not obviously deteriorate the tensile properties of the welded joint, even though there are large amount of these brittle phases in the FZ. Nevertheless, another possible explanation may be that the fine dendrite structure and fine  $\gamma''$  and  $\gamma'$  precipitation in the matrix make the FZ high in strength, and the plastic deformation in the welded joint at room temperature tensile deformation is too small to reveal the bad effects of these weak points in the welded joint. No matter which explanation is more

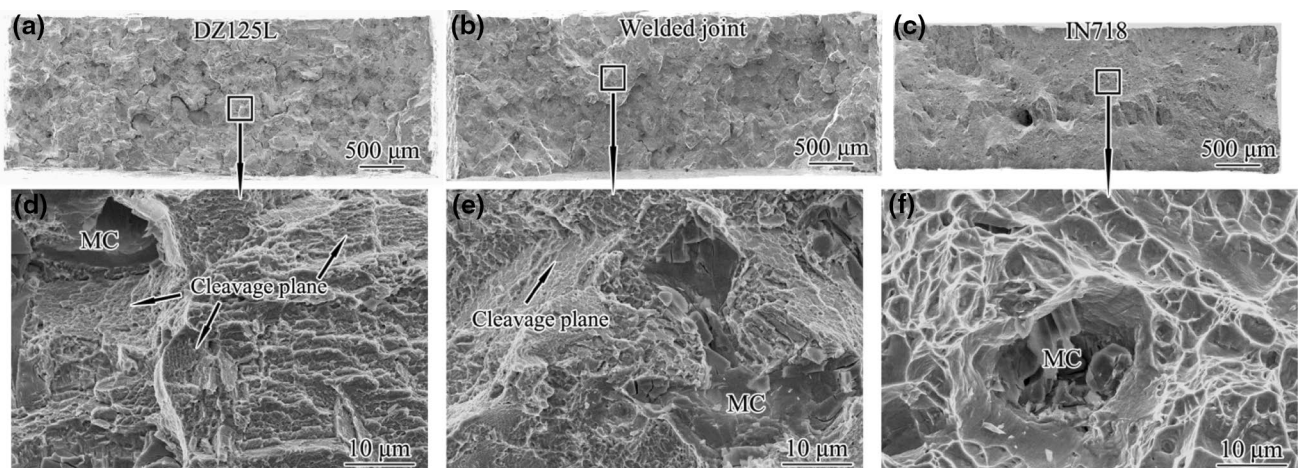


**Fig. 13** SEM micrographs showing the fracture surface morphology of the DZ125L, IN718 and the dissimilar DZ125L/IN718 welded joint after tensile deformation **a, d** DZ125L, **b, e** welded joint, and **c, f** IN718

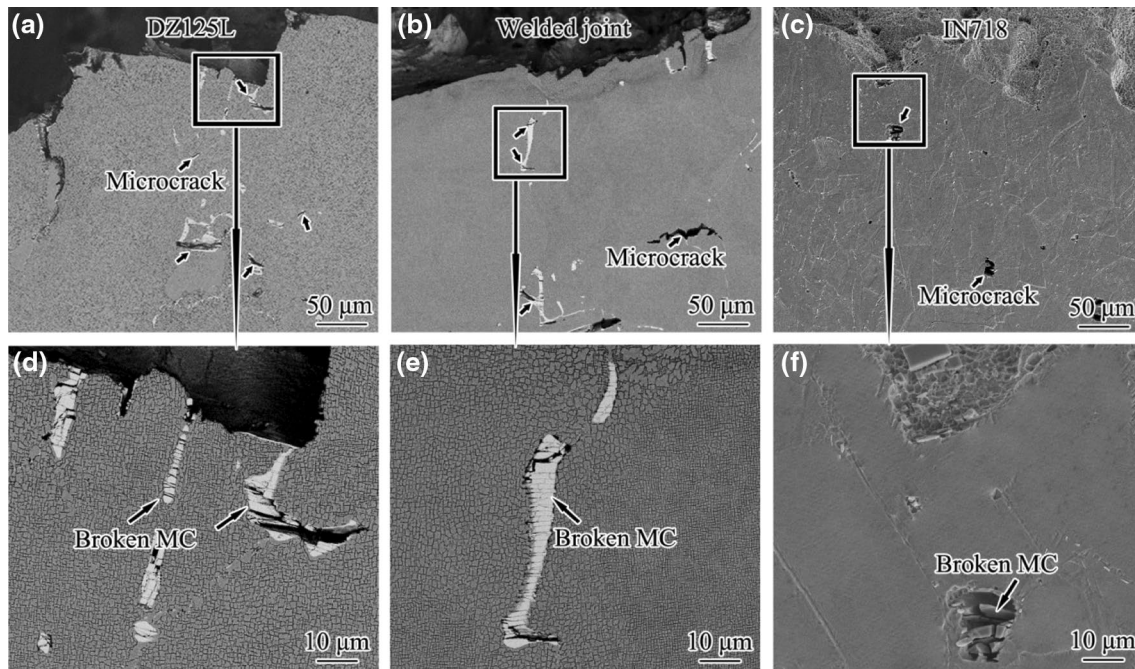


**Fig. 14** SEM micrographs showing the cross sectional surface near the fracture location of the DZ125L, IN718 and the dissimilar DZ125L/IN718 welded joint after tensile deformation **a, d** DZ125L, **b, e** welded joint, and **c, f** IN718

reasonable, the welded joint in the present study has sufficient strength comparing to the weaker DZ125L BM. Besides, the FZ has the plastic deformation capability to deform coordinately with other parts other than premature failure or obvious damage in the FZ.

## 4 Conclusions

The present work focused on the microstructure and mechanical properties of the AW and PWHT of the dissimilar welded joints of DZ125L and IN718 nickel base superalloy. The following conclusions can be drawn:

1. The FZ of the AW joint mainly consists of fine dendrite structure with a cell spacing of 5  $\mu\text{m}$  ~ 10  $\mu\text{m}$ . The incomplete mixing of base metals induces element macrosegregations during welding. The microsegregation of elements promotes the precipitation of fine  $\gamma'$  in the Al and Ti rich regions and the formation of fine Laves phases and MC carbides in the interdendrites.
2. In the HAZ of DZ125L,  $\gamma'$  partially dissolve into the matrix during welding and the dissolution is more obvious in the shoulder. In the HAZ of IN718, no obvious grain growth can be observed. Grain boundaries in both of the HAZs get liquid and Laves phases form in these boundaries.
3. After PWHT, fine  $\gamma'$  and  $\gamma''$  phases precipitate in the FZ, while the  $\gamma''$  mainly precipitate in the interdendrite of the Nb rich regions. In the BM and HAZ of DZ125L, fine  $\gamma'$  precipitate in the  $\gamma$  channel. In the BM and HAZ of IN718, both of fine  $\gamma'$  and  $\gamma''$  precipitate in the grain and along liquid grain boundaries.
4. The highest microhardness values of the AW joint are at DZ125L and the lowest are at the HAZ of IN718. There are sudden changes between the adjacent two regions. After PWHT, the microhardness of all regions increases in various degrees to almost the same values due to the precipitation of  $\gamma'$  and  $\gamma''$  phases. The relatively higher values locate at the FZ while the relatively lower values are in the region of DZ125L.
5. The YS and UTS of the welded joint are higher than the DZ125L alloy and lower than the IN718 alloy. Fracture occurs at the position within the weaker DZ125L which is away from the HAZ and FZ. The brittle MC carbides and Laves phases in the FZ do not obviously deteriorate the tensile properties of the welded joint. Since the plastic strain mainly concentrates in the region of DZ125L alloy, the welded joint shows relatively low ductility.

**Acknowledgements** This work was supported by the National Natural Science Foundation of China (51571052 and U1708253), the Science and Technology Major Project (2017-VI-0002), and the Fundamental Research Funds for the Central Universities (N160204004).

## References

1. J. Zhang, D. Zhu, Z. Xu, K. Zhang, J. Liu, N. Qu, D. Zhu, J. Mater. Process. Technol. **231**, 301–311 (2016)
2. I. Gurrappa, I.V.S. Yashwanth, J.S. Burnell-Gray, Metall. Mater. Trans. A **44**, 5270–5280 (2013)
3. D. Dye, O. Hunziker, R.C. Reed, Acta Mater. **49**, 683–697 (2001)
4. M.B. Henderson, D. Arrell, R. Larsson, M. Heobel, G. Marchant, Sci. Technol. Weld. Join. **9**, 13–21 (2013)
5. Y. Ahn, B. Yoon, H. Kim, C. Lee, Met. Mater. Int. **8**, 469–477 (2002)
6. H.N. Moosavy, M.R. Aboutalebi, S.H. Seyedein, C. Mapelli, Mater. Charact. **82**, 41–49 (2013)
7. R.K. Sidhu, O.A. Ojo, N.L. Richards, M.C. Chaturvedi, Sci. Technol. Weld. Join. **14**, 125–131 (2009)
8. R. Kayacan, R. Varol, O. Kimilli, Mater. Res. Bull. **39**, 2171–2186 (2004)
9. X. Cao, B. Rivaux, M. Jahazi, J. Cuddy, A. Birur, J. Mater. Sci. **44**, 4557–4571 (2009)
10. G. Çam, M. Koçak, Int. Mater. Rev. **43**, 1–44 (2013)
11. Y.L. Hu, X. Lin, K. Song, X.Y. Jiang, H.O. Yang, W.D. Huang, Opt. Laser Technol. **86**, 1–7 (2016)
12. H. Xiao, S.M. Li, W.J. Xiao, Y.Q. Li, L.M. Cha, J. Mazumder, L.J. Song, Mater. Lett. **188**, 260–262 (2017)
13. T. Soysal, S. Kou, D. Tat, T. Pasang, Acta Mater. **110**, 149–160 (2016)
14. K.R. Vishwakarma, N.L. Richards, M.C. Chaturvedi, Mater. Sci. Eng. A **480**, 517–528 (2008)
15. L.O. Osoba, R.G. Ding, O.A. Ojo, Mater. Charact. **65**, 93–99 (2012)
16. S.G.K. Manikandan, D. Sivakumar, K. Prasad Rao, M. Kamaraj, Mater. Charact. **100**, 192–206 (2015)
17. M. Pang, G. Yu, H.H. Wang, C.Y. Zheng, J. Mater. Process. Technol. **207**, 271–275 (2008)
18. P.F. Fu, Z.Y. Mao, J. Lin, X. Liu, C.J. Zuo, H.Y. Xu, Vacuum **102**, 54–62 (2014)
19. J.N. DuPont, J.C. Lippold, S.D. Kiser, Solid-solution strengthened Ni-base alloys. In: *Welding Metallurgy and Weldability of Nickel-Base Alloys* (Wiley, Hoboken, New Jersey, 2009), pp. 47–156
20. L. Wang, Y. Wang, Y. Liu, X. Song, X. Lü, B. Zhang, Int. J. Miner. Metall. Mater. **20**, 861–866 (2013)
21. I.J. Moore, M.G. Burke, E.J. Palmiere, Acta Mater. **119**, 157–166 (2016)
22. C. Slama, C. Servant, G. Cizeron, J. Mater. Res. **12**, 2298–2316 (1997)
23. R.A. Branun, F.J. Radavich, P.C. Stinner, in *International symposium on the metallurgy and applications of superalloy 718*, ed. by E.A. Loria, (Minerals, Metals and Materials Society, Warrendale, PA, 1989), pp. 623–629
24. A. Chamanfar, M. Jahazi, J. Cormier, Metall. Mater. Trans. A **46**, 1639–1669 (2015)
25. N. Lun, D.C. Saha, A. Macwan, H. Pan, L. Wang, F. Goodwin, Y. Zhou, Mater. Des. **131**, 450–459 (2017)
26. D. Shi, C. Dong, X. Yang, Mater. Des. **45**, 663–673 (2013)
27. H.X. Xie, C.Y. Wang, T. Yu, J. Mater. Res. **23**, 1597–1603 (2008)
28. O.A. Ojo, N.L. Richards, M.C. Chaturvedi, Metall. Mater. Trans. A **37**, 421–433 (2006)